THREE-YEAR *WILKINSON MICROWAVE ANISOTROPY PROBE* (*WMAP*)[1] OBSERVATIONS: FOREGROUND POLARIZATION

A. KOGUT,[2] J. DUNKLEY,[3] C. L. BENNETT,[4] O. DORÉ,[5,6] B. GOLD,[4] M. HALPERN,[7] G. HINSHAW,[2] N. JAROSIK,[3]
E. KOMATSU,[8] M. R. NOLTA,[5] N. ODEGARD,[2,9] L. PAGE,[3] D. N. SPERGEL,[6] G. S. TUCKER,[10]
J. L. WEILAND,[2,9] E. WOLLACK,[2] AND E. L. WRIGHT[11]

ABSTRACT

We present a full-sky model of polarized Galactic microwave emission based on 3 years of observations by the *Wilkinson Microwave Anisotropy Probe* (*WMAP*) at frequencies from 23 to 94 GHz. The model compares maps of the Stokes Q and U components from each of the five *WMAP* frequency bands in order to separate synchrotron from dust emission, taking into account the spatial and frequency dependence of the synchrotron and dust components. This simple two-component model of the interstellar medium accounts for at least 97% of the polarized emission in the *WMAP* maps of the microwave sky. Synchrotron emission dominates the polarized foregrounds at frequencies below 50 GHz, and is comparable to the dust contribution at 65 GHz. The spectral index of the synchrotron component, derived solely from polarization data, is -3.2 averaged over the full sky, with a modestly flatter index on the Galactic plane. The synchrotron emission has mean polarization fraction 2%–4% in the Galactic plane and rising to over 20% at high latitude, with prominent features such as the north Galactic spur more polarized than the diffuse component. Thermal dust emission has polarization fraction 1% near the Galactic center, rising to 6% at the anticenter. Diffuse emission from high-latitude dust is also polarized with mean fractional polarization 0.036 ± 0.011.

Subject headings: cosmic microwave background — dust, extinction — polarization — radio continuum: ISM

1. INTRODUCTION

The *Wilkinson Microwave Anisotropy Probe* (*WMAP*) has mapped the full sky in the Stokes I, Q, and U parameters on angular scales $\theta > 0.2°$ in five frequency bands centered at 23, 33, 41, 61, and 94 GHz, denoted K, Ka, Q, V, and W, respectively (Bennett et al. 2003b; Hinshaw et al. 2007). Polarized emission at microwave frequencies is dominated by foreground emission from the Galaxy, which at degree angular scales is brighter than the cosmological signal in all of the *WMAP* bands (Page et al. 2007). Extraction of cosmological information from the *WMAP* polarization data requires fitting for the astrophysical foregrounds.

Foreground polarization at microwave frequencies is dominated by a superposition of synchrotron and thermal dust emission. Synchrotron emission results from the acceleration of cosmic ray electrons in the Galactic magnetic field. For a power-law distribution of electron energies $N(E) \propto E^{-p}$ propagating in a uniform magnetic field, the resulting emission is partially polarized with fractional linear polarization

$$f_s = \frac{p+1}{p+7/3} \qquad (1)$$

aligned perpendicular to the magnetic field (Rybicki & Lightman 1979). The frequency dependence of synchrotron emission is also related to the electron energy distribution, $T(\nu) \propto \nu^{\beta}$ with spectral index

$$\beta = -\frac{p+3}{2}, \qquad (2)$$

where T is in units of antenna temperature. For spectral index $\beta \approx -3$ observed at microwave frequencies, synchrotron emission could have fractional polarization as high as $f_s \sim 0.75$. Line-of-sight and beam averaging effects will tend to reduce the observed polarization by averaging over regions with different electron energy distribution or magnetic field orientation.

Thermal dust emission can be partially polarized as prolate dust grains align with their long axis perpendicular to the magnetic field (Davis & Greenstein 1951). The dust emission efficiency is greatest along the long axis, leading to partial linear polarization perpendicular to the magnetic field (thus following the same direction as synchrotron emission). The fractional polarization depends on the grain size distribution and is typically a few percent at millimeter wavelengths (Hildebrand 1988; Hildebrand et al. 1999; Vaillancourt 2002).

Other sources of polarized emission are possible. Extragalactic radio point sources, although detected in the unpolarized temperature maps, contribute negligibly to the observed polarization on degree angular scales (Page et al. 2007). Non-thermal emission from dust via a population of small spinning grains (Draine & Lazarian 1998) or partially magnetized grains (Draine &

[1] *WMAP* is the result of a partnership between Princeton University and NASA's Goddard Space Flight Center. Scientific guidance is provided by the *WMAP* Science Team.

[2] Code 665, Goddard Space Flight Center, Greenbelt, MD 20771; alan.j.kogut@nasa.gov.

[3] Department of Physics, Jadwin Hall, Princeton University, Princeton, NJ 08544-0708.

[4] Department of Physics and Astronomy, Johns Hopkins University, 3400 North Charles Street, Baltimore, MD 21218-2686.

[5] Canadian Institute for Theoretical Astrophysics, 60 St. George Street, University of Toronto, Toronto, ON M5S 3H8, Canada.

[6] Department of Astrophysical Sciences, Peyton Hall, Princeton University, Princeton, NJ 08544-1001.

[7] Department of Physics and Astronomy, University of British Columbia, Vancouver, BC V6T 1Z1, Canada.

[8] Department of Astronomy, University of Texas, 2511 Speedway, RLM 15.306, Austin, TX 78712.

[9] ADNET Systems, 164 Rollins Avenue, Suite 303, Rockville, MD 20852.

[10] Department of Physics, Brown University, 182 Hope Street, Providence, RI 02912-1843.

[11] PAB 3-909, UCLA Physics and Astronomy, P.O. Box 951547, Los Angeles, CA 90095-1547.

Lazarian 1999) has been proposed to explain the observed correlation between far-infrared and microwave emission in the interstellar medium. While emission from spinning dust is thought to be largely unpolarized, emission from partially magnetized grains could be substantially polarized provided the grains consist of a single magnetic domain (Draine & Lazarian 1999).

Page et al. (2007) present a simple model of foreground polarization based on the 3 year *WMAP* data. Spatial templates for the synchrotron and dust emission, fit to the high-latitude sky, reduce the residual foregrounds in the corrected maps to levels below the polarization of the cosmic microwave background. This paper compares the *WMAP* polarization data to the unpolarized synchrotron and dust emission to model the polarized foregrounds, including both the spatial and frequency variation of the foregrounds over the full sky.

2. FREQUENCY SPECTRUM

The signal variance at each *WMAP* frequency band provides a simple, model-independent estimate of the frequency spectrum of polarized emission. The data is a superposition of signal (either cosmic or foreground) and noise, $T = s + n$. We estimate the signal variance

$$s^2 = \frac{\Sigma_{i\alpha} w_{i\alpha}^a w_{i\alpha}^b T_{i\alpha}^a T_{i\alpha}^b}{\Sigma_{i\alpha} w_{i\alpha}^a w_{i\alpha}^b}, \qquad (3)$$

where i is a pixel index, a and b are map indices, α denotes the Stokes Q or U maps, and w is a pixel weight. We use different weights in different regions of the sky. Pixels at low Galactic latitude are signal-dominated and use unit weight, $w_i = 1$. At high latitudes, instrument noise becomes appreciable and we use noise weight, $w_i = N_i/\sigma_0^2$ where N_i is the number of observations in pixel i and σ_0 is the noise per observation. If the variance is computed from a single map ($a = b$), instrument noise contributes a positive contribution to each pixel, $\langle T^2 \rangle = \langle (s+n)^2 \rangle = s^2 + \langle n^2 \rangle$. We avoid this noise bias by computing the cross variance using maps from different years, $a \neq b$. Uncertainties in the noise model then affect only the uncertainty in the estimated variance but not the mean value itself. We estimate the uncertainty in the computed cross-variance using Monte Carlo simulations consisting of a model signal plus noise realizations derived from a Cholesky decomposition of the noise matrices for each map (Jarosik et al. 2007). The noise simulations thus include the contribution of $1/f$ noise as well as correlations between different pixels and between the Stokes Q and U maps. We add the same simulated foreground to each noise realization prior to computing the variance, to account for the additional scatter from one realization to the next caused by the signal-noise cross term $2sn$.

Figure 1 shows the frequency spectrum of the signal variance for two regions of the sky defined by the P06 polarization mask (Page et al. 2007): the "high signal" region inside the P06 mask, dominated by the Galactic plane and north Galactic spur where signals are clearly visible in the maps, and a "low signal" region outside the P06 mask where noise is more prominent. Both regions are dominated by a power-law component $T \propto \nu^\beta$ with spectral index $\beta_s \approx -3$ consistent with synchrotron emission. The rise in variance from V band to W band (61 to 94 GHz) requires a second component with spectral index $\beta_d \approx 2$ consistent with thermal dust. The observed variance is brighter than the expected cosmic signal ($s^2 \approx 0.14 \ \mu\text{K}^2$ within 3.7° pixels) at all frequencies. Detection of a cosmic signal requires subtraction of foreground polarization (Page et al. 2007).
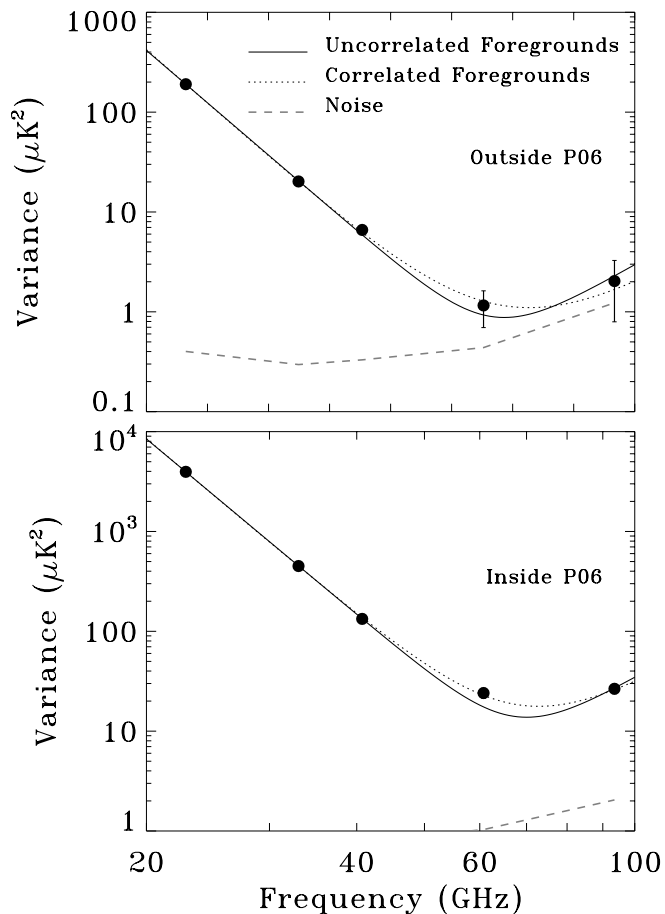

Fig. 1.—Estimated signal variance at each *WMAP* frequency band for 3.7° pixels. The solid line shows a two-component fit with power-law synchrotron and thermal dust emission assuming no spatial correlations between the two components. Allowing spatial correlations between the synchrotron and dust better reproduces the observed spectra (*dotted lines*). The dashed line shows the 68% confidence noise level. Note the change in scale between panels: the top panel shows high-latitude data outside the P06 sky mask, while the bottom panel shows data inside P06 dominated by emission from the Galactic plane.

The observed steepening of the cosmic-ray energy spectrum is expected to steepen the synchrotron emission spectrum relative to a pure power law (Müller & Tang 1987; Völk 1989). The polarization variance does not show the expected steepening above 30 GHz, but rather shows a spectrum flatter than a pure power law. This could indicate either the presence of a third emission component or nonzero spatial correlations between the synchrotron and dust components. If the synchrotron and dust components each follow a power law in frequency, $T_{\text{synch}} = S\nu_s^\beta$ and $T_{\text{dust}} = D\nu_d^\beta$, then the variance becomes

$$T^2 = S^2 \nu^{2\beta_s} + D^2 \nu^{2\beta_d} + 2rSD\nu^{\beta_s + \beta_d}, \qquad (4)$$

where r is the spatial correlation between the two components. We fit the observed variance data to a two-component model including spatial correlation, and find a broad minimum with $r \sim 0.8$ (Fig. 1, *dotted lines*). Since the unpolarized synchrotron and dust foregrounds tend to be highly correlated (Bennett et al. 2003a; Hinshaw et al. 2007), it is not surprising to find that the correlation persists in polarized emission from the same media.

3. FOREGROUND POLARIZATION

The *WMAP* 3 year data map the polarized synchrotron emission at high signal-to-noise ratio. Polarized dust emission is less

well constrained, particularly at high Galactic latitudes. We may use maps of the *unpolarized* dust to constrain the maximum amplitude of polarized dust emission. The dust polarization is

$$P_d(\hat{n}, \nu) = f_d(\hat{n})T_d(\hat{n}, \nu), \quad (5)$$

where $P = (Q^2 + U^2)^{0.5}$ is the polarized amplitude, T_d is the unpolarized amplitude, and f_d is the fractional polarization in direction $\hat{n}$. Since f_d must lie in the range [0, 1], the polarized dust amplitude cannot exceed the total unpolarized emission in any pixel.

We thus model the polarized foregrounds as a superposition of synchrotron and thermal dust emission,

$$
\begin{aligned}
Q(\hat{n}, \nu) = & P_s(\hat{n})S(\hat{n}, \nu) \cos[2\gamma_s(\hat{n})] \\
& + f_d(\hat{n})T_d(\hat{n})D(\nu) \cos[2\gamma_d(\hat{n})], \\
U(\hat{n}, \nu) = & P_s(\hat{n})S(\hat{n}, \nu) \sin[2\gamma_s(\hat{n})] \\
& + f_d(\hat{n})T_d(\hat{n})D(\nu) \sin[2\gamma_d(\hat{n})], \quad (6)
\end{aligned}
$$

where $P_s(\hat{n})$ is the (polarized) synchrotron amplitude. We model the frequency dependence of the dust as a spatially invariant power law in antenna temperature,

$$D(\nu) = \left(\frac{\nu}{\nu_0}\right)^{\beta_d}, \quad (7)$$

with spectral index $\beta_d = 2$. Synchrotron emission may be approximated as a power law, but the spectral index varies with position on the sky and may steepen with frequency. We thus model the synchrotron frequency dependence as

$$S(\nu, \hat{n}) = \left(\frac{\nu}{\nu_0}\right)^{\beta_s(\hat{n}) + C \log (\nu/\nu_0)}, \quad (8)$$

allowing the spectral index $\beta_s(\hat{n})$ to vary with position. The model includes a logarithmic steepening of the spectrum with frequency, with $C \approx -0.4$ typical of the synchrotron emission in the *WMAP* unpolarized temperature data (Hinshaw et al. 2007; Bennett et al. 2003a).

The polarization angle $\gamma(\hat{n}) = 0.5 \arctan[U(\hat{n})/Q(\hat{n})]$ is defined with respect to the Galactic meridian. Synchrotron emission dominates the lowest frequency channels, providing a template for the synchrotron polarization angle $\gamma_s(\hat{n})$. We use the 22 GHz (K band) data alone to compute the synchrotron polarization angle γ_s. In principle, this contains a small level of contamination from the cosmic signal. An alternative method computes the polarization angle from the K − Ka or K − Q difference maps. This eliminates any cosmic signal at the cost of increased noise. We use Monte Carlo simulations to compare the two methods. For noise levels typical of the *WMAP* 3 year polarization maps, direct fitting to the K-band data better reproduces the input pattern used to generate the simulations.

In this paper, we do not assume that the dust follows the same polarization direction as the synchrotron, so that the synchrotron polarization angle $\gamma_s(\hat{n})$ may differ from the dust polarization angle $\gamma_d(\hat{n})$. This allows for dust emission to originate from a different spatial distribution compared to synchrotron emission along each line of sight. We adopt the dust polarization angles from the starlight model described in Page et al. (2007) and compare this model to one in which $\gamma_d = \gamma_s$ everywhere on the sky.

The foreground model does not assume that the synchrotron spectral index is identical along all lines of sight, but fits a map of the spectral index as described in § 3.1. Given the polarization angles $\gamma_s(\hat{n})$ and $\gamma_d(\hat{n})$ and the map of the synchrotron spectral index $\beta_s(\hat{n})$, we fit the *WMAP* 3 year band-averaged polarization maps to derive the polarized synchrotron amplitude $P_s(\hat{n})$, synchrotron spectral correction C, and the dust fractional polarization $f_d(\hat{n})$ (eq. [6]). Based on signal to noise, we fit these parameters simultaneously but on different angular scales. Synchrotron emission dominates the low-frequency data. We fit for the synchrotron amplitude $P_s(\hat{n})$ (normalized to K band) in each of 3072 equal area pixels at HEALPix resolution 4 or $N_{\text{side}} = 16$ (Górski et al. 2005). Polarized dust emission is considerably fainter than synchrotron in the *WMAP* frequency bands. We thus fit for the dust fractional polarization $f_d(\hat{n})$ in six coarse sky regions, holding f_d constant within each region while simultaneously fitting for the synchrotron amplitude in each of the smaller HEALPix pixels. We fit for the synchrotron spectral correction C in two regions defined by the P06 polarization mask: one value for the high-latitude region outside the mask and an independent value for the low-latitude region inside the mask. We model the unpolarized dust emission $T_d(\hat{n}, \nu)$ using the Finkbeiner et al. (1999) model 8, evaluated at 94 GHz and scaled with uniform spectral index $\beta_d = 2$. The results do not depend sensitively on the choice for β_d.

3.1. *Polarized Synchrotron Model*

Synchrotron emission may be approximated as a power law in antenna temperature, with spectral index $\beta_s(\hat{n})$ varying with position across the sky. Hinshaw et al. (2007) present a maximum entropy model of unpolarized synchrotron emission derived from *WMAP* data. We may use this maximum entropy model to specify the frequency dependence of the polarized synchrotron emission, including both the spatial variation and the steepening of the spectrum with respect to a pure power law. The unpolarized maximum entropy model, however, suffers from confusion with free-free emission, particularly at low Galactic latitudes.

Synchrotron emission dominates the polarization data at 22 and 33 GHz (K and Ka bands), with negligible contribution from thermal dust (Fig. 1). We thus use the *WMAP* polarization data at K and Ka bands to map the synchrotron spectral index $\beta_s(\hat{n})$. We fit for the spectral index in each of 3072 pixels, imposing a uniform prior $-4.0 < \beta_s < -2.0$ to reduce the effects of instrument noise. The resulting map is still noise dominated, particularly at high latitude. We further reduce the noise contribution by smoothing the spectral index map using a top-hat window function. We select the top-hat radius and verify the accuracy of the fitting procedure using Monte Carlo realizations consisting of a fixed Galactic signal added to random realizations of instrument noise. At each pixel, we smooth the spectral index maps from each realization using a progressively larger top-hat radius, until the standard deviation of the ensemble of smoothed realizations, evaluated at that pixel, falls below a threshold $\delta\beta_s(\hat{n}) < 0.1$. The resulting smoothing radius varies across the sky from $7°$ near the plane to $18°$ at high latitude.

We investigate the dependence of the recovered spectral index map on the prior imposed during the pixel-by-pixel fit. Changing the prior to a wider range $-4.5 < \beta_s < -1.5$ or a narrower range $-3.5 < \beta_s < -2.5$ produces a systematic shift $\delta\beta_s \approx 0.1$ in the mean of the smoothed spectral index map, comparable to random uncertainty, but does not significantly alter the structure on smaller angular scales. Our choice of prior is informed by Monte Carlo realizations, where the ensemble average of the smoothed realizations accurately recovers the noiseless spectral index map used to generate the simulations.

Figure 2 shows the polarized synchrotron spectral index from the *WMAP* 3 year data. The mean value averaged over the full
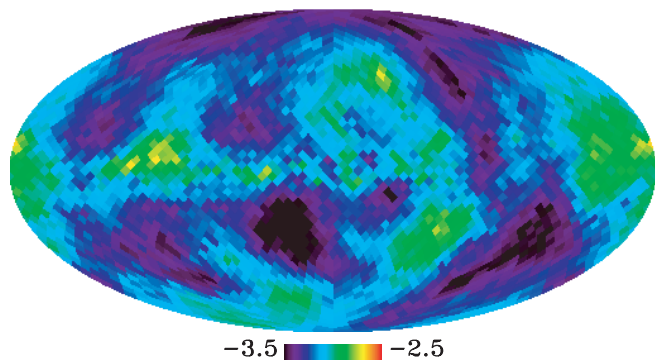
FIG. 2.—Spectral index of polarized synchrotron emission between 22 and 33 GHz (Mollweide projection in Galactic coordinates). The map has been smoothed with a position-dependent top hat varying from $7°$ radius near the plane to $18°$ radius at high latitude.

sky is $\langle \beta_s \rangle = -3.2$. The spectral index is flatter along the Galactic plane with steeper values at higher latitude. Figure 3 shows the polarization spectral index binned by Galactic latitude.

The smoothing applied to the spectral index maps creates spatial correlations in the smoothed maps. We account for this in Figure 3 by plotting the effective uncertainty in the binned data, $\delta \beta_s^{\mathrm{eff}} = \sigma_i / (N_i^{\mathrm{eff}})^{1/2}$, where σ_i is the standard deviation of the smoothed values from all pixels in the ith latitude bin, and N_i^{eff} is the number of independent spatial regions within that bin. The spectral index steepens from $\beta_s \approx -3.05$ along the plane to $\beta_s \approx -3.25$ at latitude $|b| > 30°$. Polarization data provide a measurement of the synchrotron spectral index independent of the temperature data and not subject to confusion from competing emission mechanisms.

Figure 4 shows the model polarized synchrotron emission. The polarized synchrotron amplitude $P_s(\hat{n})$ is dominated by the lowest frequency data and is nearly identical to the K-band map. We derive the synchrotron fractional polarization by comparing the K-band model amplitude to the unpolarized K-band maximum entropy synchrotron model (Hinshaw et al. 2007), assuming that this model accurately represents the unpolarized synchrotron amplitude. Although the Galactic plane dominates the polarized emission in the maps, the corresponding fractional polarization is low, indicative of contributions from multiple emitting regions along the line of sight. The north Galactic spur and its southern extension are more prominent in polarization than in intensity, indi-
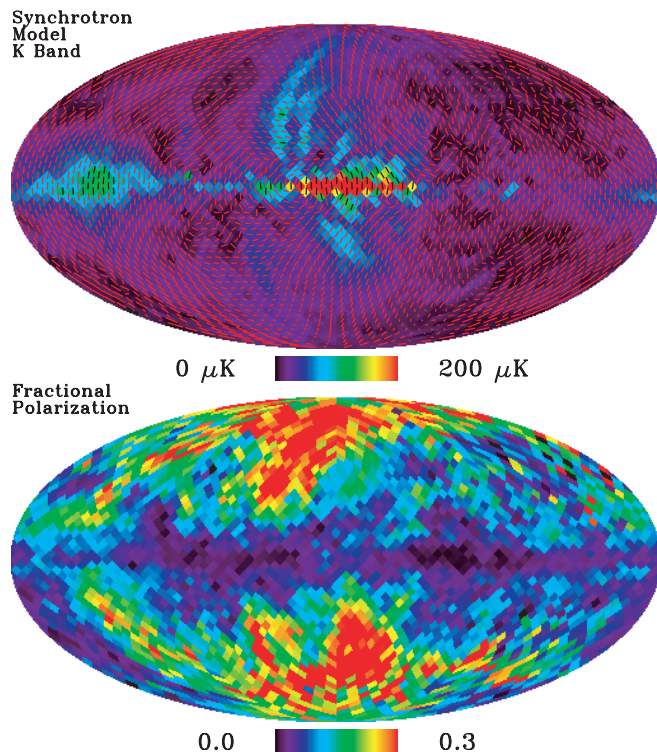
FIG. 4.—Polarized synchrotron model parameters. *Top*: Antenna temperature $P = (Q^2 + U^2)^{0.5}$ of polarized synchrotron emission at K band. Vectors indicate the polarization direction. *Bottom*: Synchrotron fractional polarization, derived by dividing the polarized model by the unpolarized maximum entropy synchrotron model at K band. The polarization fraction is 3%–5% on the Galactic plane, increasing above 20% within the north Galactic spur and its southern extension.

cating localized enhancements in the polarization fraction. Figure 5 shows a histogram of the synchrotron fractional polarization for several regions of the sky. The Galactic plane ($|b| < 5°$) is less than 10% polarized, with mode $f_s = 0.02$ and mean $f_s = 0.05$. The north Galactic spur has enhanced fractional polarization, $f_s \approx 0.3$, while the high-latitude sky outside the P06 mask has mode $f_s = 0.14$ and mean $f_s = 0.15$.

Figure 6 shows the fractional polarization binned by Galactic latitude. Within narrow latitude bins, the distribution of observed fractional polarization values approximates a Gaussian distribution. Figure 6 shows the mean $\langle f_i \rangle$ within the ith bin with uncertainty $\delta f_i = \sigma_i / (N_i)^{1/2}$ defined by the standard deviation σ_i of the N_i pixels within that bin. The uncertainties thus reflect the precision to which the mean may be defined within each latitude bin, which average over a larger range of fractional polarization (cf. Fig. 5). The mean fractional polarization rises linearly from 4% near the plane to 20% at latitude $|b| > 50°$. The north polar cap region is more polarized than the south polar cap, although this may be an artifact of the unpolarized synchrotron model used to define the synchrotron fractional polarization. Both the low polarization in the plane of the Galaxy and the trend toward higher fractional polarization at high latitude are similar to previous measurements of external spiral galaxies. Edge-on spirals typically exhibit 1%–3% polarization in the disk, rising linearly to 10%–20% at distances of several kiloparsecs from the major axis (Hummel et al. 1991; Sukumar & Allen 1991; Dumke et al. 1995, 2000; Dumke & Krause 1998). The large-scale polarization of the Milky Way is thus unremarkable compared to other galaxies.

The foreground model directly fits the polarized synchrotron amplitude $P_s(\hat{n})$ and compares this fitted amplitude to a model of
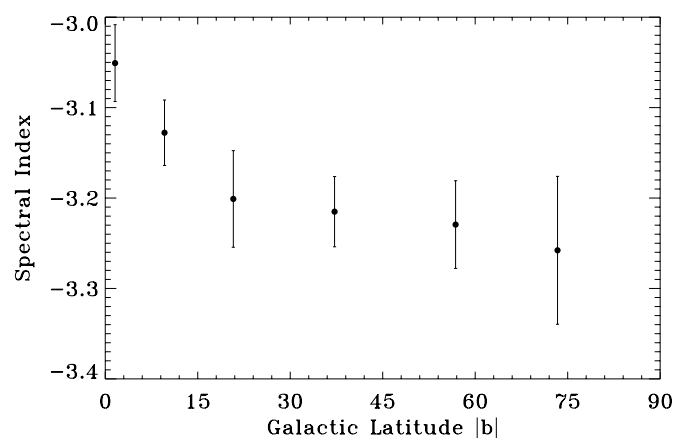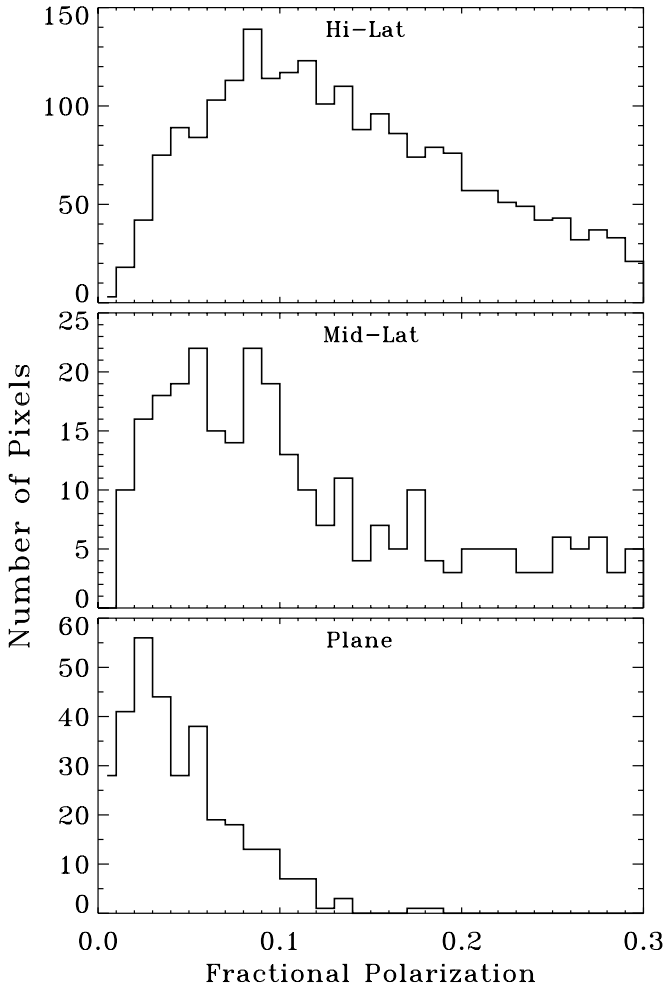

FIG. 3.—Spectral index of polarized synchrotron emission binned by Galactic latitude. The spectral index steepens off the Galactic plane. Similar behavior is observed in external edge-on spiral galaxies.

Fig. 5.—Histogram of synchrotron fractional polarization f_s. *Top*: High-latitude region outside the P06 mask. *Middle*: Midlatitude region inside P06 but with $|b| > 5°$. *Bottom*: Galactic plane, $|b| < 5°$.

the unpolarized synchrotron emission to estimate the fractional polarization f_s. A recent comparison of the unpolarized *WMAP* K-band map at 22 GHz with a full-sky map at 19 GHz suggests that much of the emission near the Galactic plane results from a component spatially correlated with thermal dust emission but
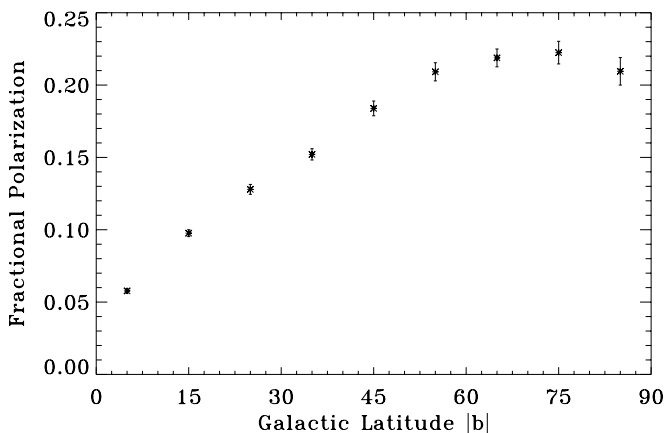

Fig. 6.—Synchrotron fractional polarization f_s binned by Galactic latitude for the northern (*filled symbols*) and southern (*open symbols*) hemispheres. Each point shows the mean fractional polarization f_s for all pixels in a latitude bin with signal-to-noise ratio greater than 1. The error bars show the uncertainty in the mean based on the scatter of values within each latitude bin.

TABLE 1
Dust Fractional Polarization

Region	Galactic Latitude (deg)	Galactic Longitude (deg)	Fractional Polarization f_d
1............	−10 to 10	−135 to −45	0.010 ± 0.003
2............	−10 to 10	−45 to 45	0.010 ± 0.005
3............	−10 to 10	45 to 135	0.012 ± 0.005
4............	−10 to 10	135 to −135	0.064 ± 0.013
5............	$|b| > 10$, inside P06		0.020 ± 0.014
6............	Outside P06		0.036 ± 0.011

with spectral index $\beta \approx -1.7$, consistent with spinning dust (Boughn & Pober 2007). To the extent that the maximum entropy synchrotron model overestimates the unpolarized synchrotron amplitude by ignoring spinning dust, the fractional polarization f_s derived above becomes a lower limit to the true synchrotron fractional polarization. Since the values for f_s derived using the maximum entropy model agree with observations of external edge-on spiral galaxies at much lower frequencies (where spinning dust is negligible), requiring a substantial fraction of the unpolarized emission at 22 GHz to originate from spinning dust would require some compensating depolarization of the synchrotron component (e.g., line-of-sight effects or a tangled magnetic field) to keep the Milky Way in family with similar external galaxies.

3.2. *Polarized Dust Model*

Polarized dust emission is brighter than synchrotron only in the highest frequency channel, and only significantly so on the Galactic plane. Since the dust fractional polarization f_d is by definition positive, noise in the W-band data can create a positive bias in the fitted dust solution. We estimate this bias using Monte Carlo simulations, comparing the recovered synchrotron and dust parameters to known inputs in each coarse sky region for 300 realizations consisting of synchrotron, dust, CMB, and instrument noise generated using Cholesky decomposition of the full noise matrix in each DA (differencing assembly; Jarosik et al. 2007). The recovered dust solution is nearly identical to the input, with bias less than 10% of the statistical uncertainty. We do not apply a correction for this effect.

Table 1 shows the fractional polarization of the dust in each coarse sky region. The fractional polarization in the plane increases away from the Galactic center, with $f_d = 0.01$ at the Galactic center rising to 0.06 at the anticenter. The fractional polarization increases with latitude, reaching a value $f_d = 0.036 \pm 0.011$ outside the P06 polarization mask.

Equation (6) fits a single parameter to the high-latitude dust (outside the P06 mask). We have repeated the fit using more "coarse" sky regions outside the P06 mask. The faint amplitude of the dust signal combined with the lack of small-scale structure in the high-latitude template map $D(\hat{n})$ prevent a statistically significant determination of substructure in the high-latitude polarized dust signal.

4. DISCUSSION

We model the polarized foreground emission in each pixel as a superposition of synchrotron emission with spatially variable spectral index determined from the *WMAP* polarization data plus dust emission traced by the Finkbeiner et al. (1999) dust model scaled by a spatially variable fractional polarization. Figure 7 shows the model and residuals for each frequency band. A simple test compares the variance of the foreground-cleaned maps to
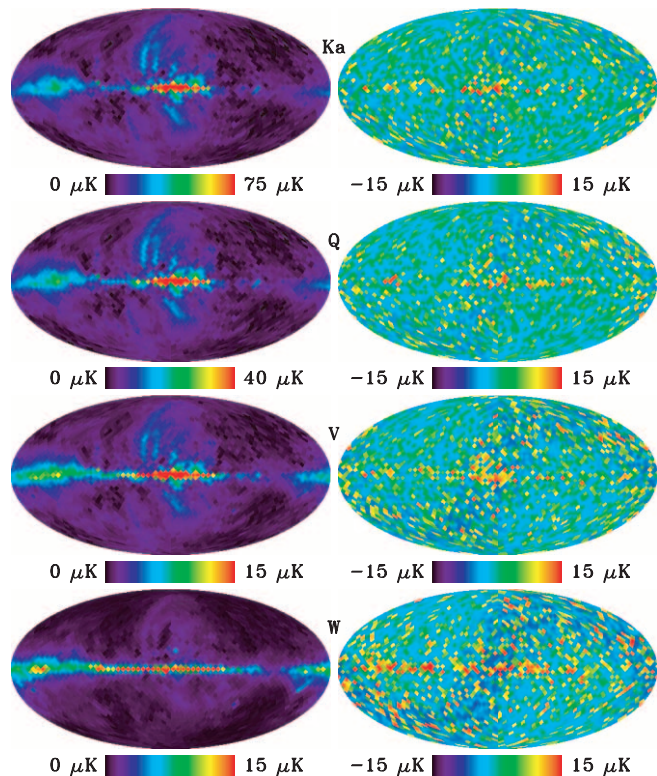
Fig. 7.—Polarized foreground model and residuals for the pixel-by-pixel polarization model. *Left*: Antenna temperature of polarized emission at each band. The polarization direction is not shown. *Right*: Residuals after subtracting foreground model. For visualization, the residuals $P = (Q^2 + U^2)^{1/2}$ are shown, corrected for the positive noise bias using Monte Carlo simulations. The model and χ^2 are computed directly from the Stokes Q and U maps.

TABLE 2
χ^2 OF RESIDUAL MAPS

Band	χ^2	dof	χ^2/dof
Pixel Model, Outside P06			
Ka..........................	4604	4524	1.018
Q..........................	4521	4524	1.000
V..........................	4600	4524	1.017
W..........................	4774	4524	1.055
All	18505	18098	1.023
Pixel Model, Inside P06			
Ka..........................	1626	1601	1.016
Q..........................	1541	1601	0.963
V..........................	1670	1601	1.043
W..........................	1773	1601	1.107
All	6611	6404	1.032
Template Model, Outside P06			
Ka..........................	4968	4532	1.096
Q..........................	4616	4532	1.019
V..........................	4608	4532	1.017
W..........................	4760	4532	1.050
All	18952	18128	1.045
Template Model, Inside P06			
Ka..........................	2403	1608	1.494
Q..........................	2081	1608	1.294
V..........................	2704	1608	1.682
W..........................	4946	1608	3.076
All	12034	6432	1.871

the variance of the uncleaned maps (eq. [3]). The foreground model removes over 97% of the power at Ka and Q bands where foregrounds are brightest. Outside the P06 mask, the variance of the cleaned maps is close to the value expected for instrument noise alone.

Table 2 compares the template model described in Page et al. (2007) to the pixel model described in this paper, using goodness-of-fit statistic

$$\chi^2 = \Sigma_{ij\alpha\beta} R_{i\alpha} N^{-1}_{ij\alpha\beta} R_{j\beta}, \qquad (9)$$

where N^{-1} is the inverse noise matrix and $R_{i\alpha}$ is the (data − model) residual in pixel i and Stokes parameter α. The synchrotron amplitude P_s and polarization angle γ_s in the pixel model are derived almost entirely from the K-band data, leaving nearly zero residuals at K band. Since the synchrotron amplitude and polarization angle may be treated as an external (K band) template, we assess the goodness of fit using only the four higher frequency bands, counting only the parameters fitted using data at these bands. The high-latitude region outside the P06 mask contains 2267 pixels in each of the Stokes Q and U maps in each of the four frequency bands. The synchrotron spectral index map has 36 independent regions outside the P06 mask (after accounting for smoothing), requiring 36 parameters in the extended model. We add one additional parameter for the synchrotron spectral correction C plus another for the dust fractional polarization f_d to obtain a total of 38 parameters fitted to 18,136 data points outside the P06 mask. For the 805 pixels inside the P06 mask we fit 31 parameters for the synchrotron spectral index, five parameters

for dust, plus one parameter for the synchrotron spectral correction for a total of 36 parameters fitted to 6440 low-latitude data points. The template model, by comparison, fits only two parameters to each band, one each for the dust and synchrotron template maps.

Fitting a spatially variable synchrotron spectral index provides a statistically significant improvement ($\Delta\chi^2 = 447$ for 30 additional model parameters outside the P06 mask) compared to the template model, which assumes the same spatial pattern for the synchrotron at all bands. Most of this improvement comes at Ka and Q bands where synchrotron is brightest. Although the pixel-based model has a lower χ^2 at V band, the difference at this band alone is not statistically significant. The template model has slightly better χ^2 at W band outside the P06 mask. Not surprisingly, the pixel-based model provides a better fit at all bands inside the P06 mask.

The pixel-based model finds a synchrotron spectrum marginally flatter than a power law, with best-fit spectral correction $C = 0.3 \pm 0.1$. This result is unchanged with modifications of the model (polarization angle, synchrotron spectral index map, dust spectral index) and is independent of the sky cut. The apparent flattening is a robust feature of the data, derived independently from analyses of the data variance (§ 2), the pixel-based model (§ 3), and the template model (Page et al. 2007). We obtain the same value for C fitted independently to the regions inside and outside the P06 mask. We note that the value for C is heavily weighted by the data at Q and V bands, where both the synchrotron and dust are faint. Forcing $C = 0$ to fit a pure power law increases the χ^2 by 10 outside the P06 mask, while a steepening spectrum ($C = -0.4$) increases χ^2 by 45. In both cases the fitted dust parameters shift slightly compared to the best-fit model. We define a systematic

uncertainty for the dust fractional polarization as the change in f_d induced as the synchrotron spectral correction parameter C varies from 0.3 to -0.4. The uncertainties reported in Table 1 include this systematic uncertainty added in quadrature with the statistical uncertainty.

The χ^2 analysis quantifies the dependence of the synchrotron spectral index map on the choice of prior used in the fitting process (§ 3.1). We repeat the full foreground analysis, replacing the spectral index map $\beta_s(\hat{n})$ in equations (6)–(8) with a new map derived using a different prior before recomputing the best-fit values for the foreground model. We find a broad minimum in χ^2 near prior $-4.0 < \beta_s < -2.0$, consistent with the Monte Carlo tests described in § 3.1. Changing to a more restrictive prior $-3.5 < \beta_s < -2.5$ increases χ^2 by 33, while the looser prior $-4.5 < \beta_s < -1.5$ increases χ^2 by 2.

A χ^2 test confirms that the structure in the synchrotron spectral index map is dominated by a steepening of the spectral index off the Galactic plane. We create a map of the synchrotron spectral index in which the value at each pixel depends only on Galactic latitude (first four bins from Fig. 3). We then compare the foreground model derived using this spectral index map to a model derived using a uniform spectral index equal to the mean of the best-fit spectral index map. Allowing the spectral index to vary with latitude near the plane improves the χ^2 by 88 using only four additional parameters.

We also test the assumption that the polarized dust distribution may be traced by the polarization angle derived from observations of polarized starlight. We repeat the fit in equation (6), replacing the dust polarization angle γ_d with the synchrotron polarization angle γ_s derived from the WMAP K-band data. The fit is marginally better ($\Delta\chi^2 = 9$) when the polarized dust emission follows the magnetic field inferred from polarized starlight instead of the magnetic field derived from the synchrotron component.

We may also use the polarization data to constrain emission from any additional component such as spinning dust. Direct comparison of the polarized maps yields spectral index $\beta_s \approx -3.05$ near the Galactic plane, consistent with synchrotron emission but inconsistent with the inverted spectrum found by Boughn & Pober (2007). We test for polarized emission traced by the dust morphology by modifying equation (6) to include additional terms

$$Q_{\rm spin}(\hat{n},\ \nu) = f_{\rm spin}(\hat{n})T_d(\hat{n})D_{\rm spin}(\nu)\cos[2\gamma_d(\hat{n})],$$
$$U_{\rm spin}(\hat{n},\ \nu) = f_{\rm spin}(\hat{n})T_d(\hat{n})D_{\rm spin}(\nu)\sin[2\gamma_d(\hat{n})],\quad (10)$$

where $f_{\rm spin}$ is the fractional polarization of the spinning dust component with frequency dependence $D_{\rm spin}(\nu)$ peaking near 20 GHz (Draine & Lazarian 1998). We repeat the fit using either a spatially invariant synchrotron spectral index or the spatially variable map of polarized synchrotron emission derived from the K–Ka band comparison (Fig. 2). We fit the spinning dust term within the same coarse pixels as the thermal dust emission, but make no assumption concerning the relative amplitudes of the thermal vs spinning dust components. In all cases, the fitted values are consistent with no spinning dust contribution to the polarization data, $f_{\rm spin} = 0$. Spinning dust contributes less than 1% of the observed polarization signal variance in any band.

Page et al. (2007) analyzed the WMAP polarization data outside the P06 mask to detect a cosmic signal at amplitude $l(l+1)C_l^{\rm EE}/2\pi = 0.086 \pm 0.029\ \mu{\rm K}^2$ averaged over multipole moments $l = 2$–6. Their analysis used a foreground model derived by fitting template maps to the high-latitude portion of the WMAP Stokes Q and U data. This paper extends the foreground model to
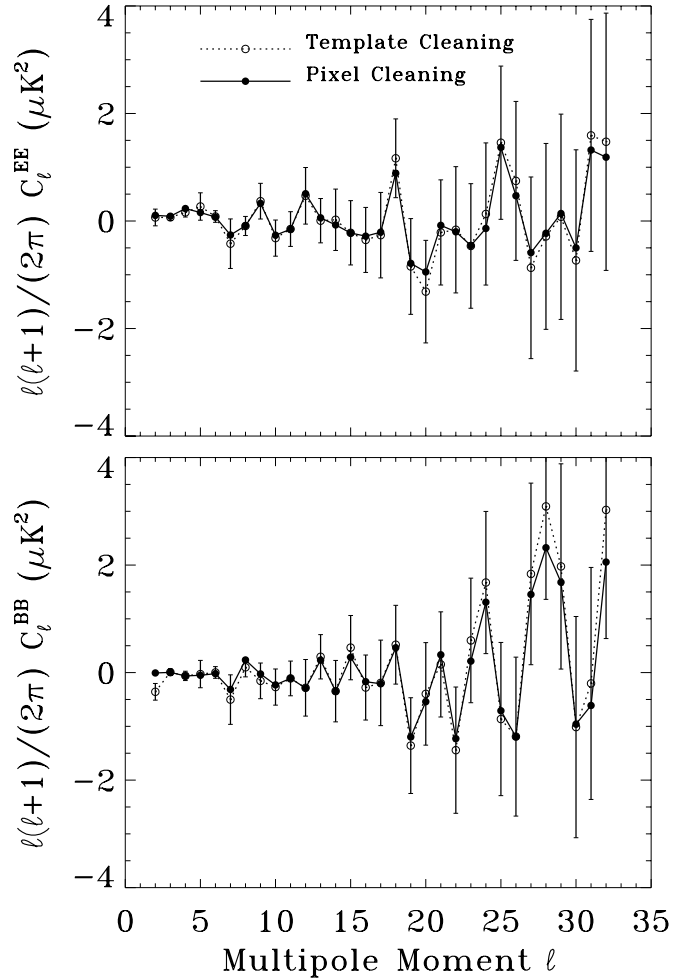

Fig. 8.—CMB power spectra outside the P06 mask, derived from Q- and V-band data after subtracting two different foreground models. *Top*: EE power spectra. *Bottom*: BB power spectra. The CMB spectra are robust with respect to different foreground models.

include spatial variation and frequency dependence of the synchrotron spectral index along with spatial variation in the dust fractional polarization. The extended foreground model allows an improved understanding of the astrophysical foregrounds but does not significantly alter the cosmological conclusions. Fitting the variance of the residual maps as a superposition of instrument noise plus a cosmological signal yields a best-fit value $s^2 = 0.38 \pm 0.21\ \mu{\rm K}^2$ for the CMB variance in thermodynamic temperature units, compared to the expected value $s^2 = 0.14\ \mu{\rm K}^2$ derived from the Page et al. (2007) detection.

The cross variance analysis provides a simple, model-independent limit to residual signals in the cleaned maps. Errors in the instrument noise model affect the quoted uncertainty but do not bias the fitted value. However, the variance analysis does not account for spatial correlations in the instrument noise. We have repeated the likelihood analysis by correcting the Q- and V-band polarization maps using the pixel-based foreground model instead of the template model. Figure 8 shows the power spectra of the CMB signal outside the P06 mask, derived from the weighted sum of the cleaned cross spectra at Q and V bands on angular scales up to the pixel size (cf. Fig. 21 of Page et al. 2007). The two cleaning techniques produce nearly identical results; the only change larger than the noise uncertainty is for the BB power spectrum at multipole moment $l = 2$. We quantify the effect of different foreground cleaning on cosmological parameter estimation by jointly fitting

the EE and TE data using the stand-alone likelihood code without foreground marginalization as described in Page et al. (2007, Table 9). Changing the foreground model moves the fitted value for the optical depth from $\tau = 0.092^{+0.029}_{-0.030}$ to $\tau = 0.098$, a shift of roughly a fifth of the uncertainty. Systematic uncertainties in cosmological parameters caused by the foreground polarization are small compared to the noise levels of the *WMAP* 3 year data.

5. CONCLUSIONS

WMAP detects polarized emission over the full microwave sky. The frequency dependence of this emission is consistent with a superposition of polarized synchrotron and thermal dust emission. A pixel-by-pixel fit to the Stokes Q and U maps from the band-averaged 3 year data separates the emission into synchrotron and dust components. Synchrotron emission dominates the polarization below frequencies of about 60 GHz. The spectral index of the synchrotron component, derived solely from polarization data, is -3.2 averaged over the full sky, with a modestly flatter index on the Galactic plane. Comparison of the polarized synchrotron emission to a maximum entropy model of the unpolarized emission shows typical fractional polarization of 2%–4%

near the Galactic plane, rising to 20% at latitude $|b| > 50°$. Prominent structures such as the north Galactic spur appear as localized enhancements in the polarization fraction. We detect polarized dust emission with fractional polarization increasing from a minimum of 1% near the Galactic center to 6% at the anticenter. Diffuse emission from high-latitude dust is also polarized with mean fractional polarization 0.036 ± 0.011. This simple two-component model of the interstellar medium accounts for at least 97% of the polarized emission in the *WMAP* maps of the microwave sky.

REFERENCES

Bennett, C. L., et al. 2003a, ApJS, 148, 97
———. 2003b, ApJS, 148, 1
Boughn, S. P., & Pober, J. C. 2007, ApJ, 661, 938
Davis, L. J., & Greenstein, J. L. 1951, ApJ, 114, 206
Draine, B. T., & Lazarian, A. 1998, ApJ, 494, L19
———. 1999, ApJ, 512, 740
Dumke, M., & Krause, M. 1998, in The Local Bubble and Beyond, ed. D. Breitschwerdt, M. J. Freyberg, & J. Truemper (Berlin: Springer), 555
Dumke, M., Krause, M., & Wielebinski, R. 2000, A&A, 355, 512
Dumke, M., Krause, M., Wielebinski, R., & Klein, U. 1995, A&A, 302, 691
Finkbeiner, D. P., Davis, M., & Schlegel, D. J. 1999, ApJ, 524, 867
Górski, K. M., Hivon, E., Banday, A. J., Wandelt, B. D., Hansen, F. K., Reinecke, M., & Bartlemann, M. 2005, ApJ, 622, 759

Hildebrand, R. H. 1988, QJRAS, 29, 327
Hildebrand, R. H., Dotson, J. L., Dowell, C. D., Schleuning, D. A., & Vaillancourt, J. E. 1999, ApJ, 516, 834
Hinshaw, G., et al. 2007, ApJS, 170, 288
Hummel, E., Beck, R., & Dahlem, M. 1991, A&A, 248, 23
Jarosik, N., et al. 2007, ApJS, 170, 263
Müller, D., & Tang, K. 1987, ApJ, 312, 183
Page, L., et al. 2007, ApJS, 170, 335
Rybicki, G. B., & Lightman, A. 1979, Radiative Processes in Astrophysics (New York: Wiley)
Sukumar, S., & Allen, R. 1991, ApJ, 382, 100
Vaillancourt, J. E. 2002, ApJS, 142, 53
Völk, H. J. 1989, A&A, 218, 67